Engineering Structures 309 (2024) 118077

Contents lists available at ScienceDirect

Engineering Structures

journal homepage: www.elsevier.com/locate/engstruct

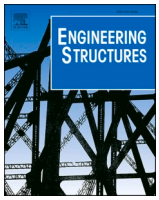

Seismic response prediction and parameters estimation of the frame structure equipped with the base isolation-fluid inerter system (FS-BIFI) based on the PI-LSTM model

Yangyang Liao [a], Hesheng Tang [a,*], Rongshuai Li [b], Lingxiao Ran [a], Liyu Xie [a]

[a] Department of Disaster Mitigation for Structures, College of Civil Engineering, Tongji University, Shanghai 200092, China
[b] Shanghai Construction Group Co., Ltd., Shanghai 200080, China

ARTICLE INFO

Keywords:
Response prediction
Parameters estimation
FS-BIFI
PI-LSTM
Fluid inerter
Anti-toppling rolling base isolation

ABSTRACT

This paper introduces a novel approach, the physics-informed long short-term memory (PI-LSTM) model, to address the forward and inverse problems of the frame structure equipped with the base isolation-fluid inerter system (FS-BIFI). Validation of the PI-LSTM model's effectiveness is demonstrated through a numerical case study of a single-story FS-BIFI. Employing this approach, the PI-LSTM model accurately predicted displacement and acceleration responses of a three-story FS-BIFI. Moreover, it conducts an evaluation of unknown damping-related parameters (β_1, β_2) and a stiffness-related parameter (μ) of the fluid inerter mounted on the FS-BIFI. The model demonstrates a robust confidence value of 96.68% in predicting response error values within the range of [− 10%, 10%]. Notably, the relative errors in estimating unknown parameters (β_1, β_2, μ) stand at 12.760%, 8.857%, and 3.750%, respectively. The results show that the PI-LSTM model has great potential for response prediction and parameter inversion of complex structural systems.

1. Introduction

Earthquakes are sudden and destructive natural disasters. The safety and performance of structures under seismic forces constitute a crucial topic in the field of earthquake engineering, directly impacting human safety, property loss, and societal stability [1,2]. Therefore, it is very important to monitor the health status of the structure under excitation, and the structural response is one of the most commonly used indicators. In order to mitigate the extent of structural damage under seismic effects, engineering practices often employ seismic isolation devices or vibration reduction devices, such as hydraulic dampers and friction isolators. The inerter, serving as a novel seismic device, is progressively being utilized in conjunction with other devices (such as isolators) in the realm of earthquake engineering [3,4]. The structures equipped with vibration reduction or isolation devices exhibit strong nonlinear characteristics in response to external loads. This nonlinear behavior constitutes a substantial threat to structural stability and reliability. Therefore, conducting comprehensive analyses and assessments of these nonlinear traits stands as an imperative [5,6].

A large number of scholars have conducted a large number of studies on the vibration characteristics of structures under earthquake action [7–9]. Li et al. [10] investigated the reduced model and seismic response of inter-story isolated buildings by establishing equations of motion utilizing modal displacements of linear lower and upper structures. Xiong et al. [11] investigated the nonlinear stochastic dynamic nature of submerged floating tunnels (SFT) under seismic excitation, deriving their differential equations and assessing their seismic performance through dynamic reliability analysis. Malik et al. [12] investigated the dynamic characteristic of a viscously damped outrigger system in a 60-story tall building under seismic and wind loads. Dynamic response analysis of structures stands as a pivotal component in seismic engineering. With increasingly complex application scenarios, the structural response triggered by earthquakes exhibits diverse and intricate characteristics, hence the continued in-depth exploration in related studies.

Benefiting from the advancements in experimental methodologies, sensor technologies, and numerical techniques, a vast amount of data is being generated, collected, and processed. Data-driven methods have also developed rapidly in structural response modeling. Traditional data-driven deep learning (DL), such as convolutional neural networks (CNN), long short-term memory (LSTM) neural networks, utilizes algorithms to parse data, learning hidden information and physical knowledge from the data, subsequently making decisions or predictions

* Corresonding author.
E-mail address: thstj@tongji.edu.cn (H. Tang).

https://doi.org/10.1016/j.engstruct.2024.118077
Received 22 December 2023; Received in revised form 9 March 2024; Accepted 21 April 2024
Available online 2 May 2024

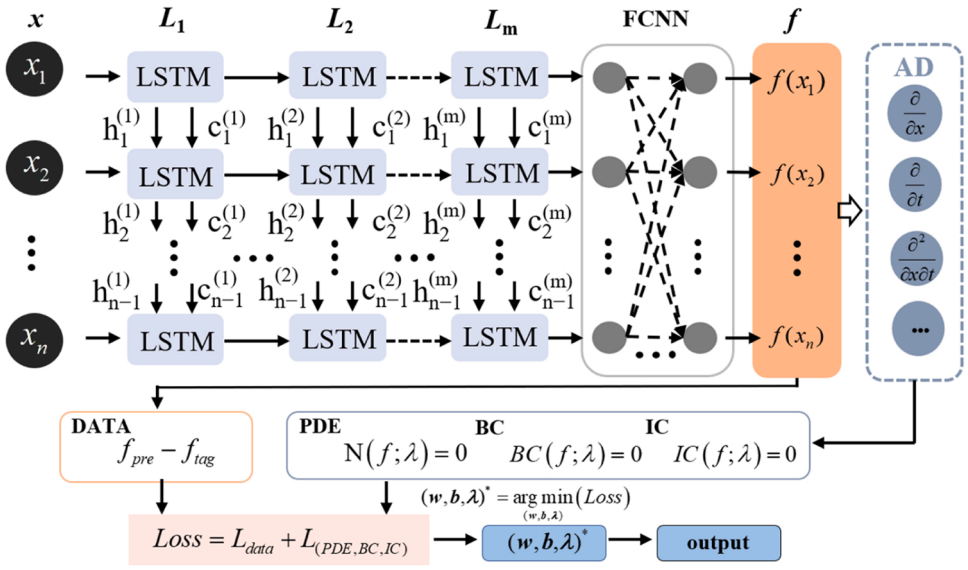

Fig. 1. The schematic diagram of PI-LSTM.

[13–15]. Recent research has also confirmed that optimizing standard neural network architectures for compositional skills can achieve a level of systematicity similar to that of humans [16]. However, this method relies on extensive labeled data to maintain the model's generalization ability and high-performance output, resulting in poor generalization and interpretability of the model.

In order to overcome the limitations of the aforementioned methods, a physics-driven deep learning (PDDL) paradigm, which combines data-driven DL models with physics-driven computational mechanics models, has been proposed [17–20]. Subsequently, PDDL paradigm has been further optimized [21–25] and has been extensively applied in fields including structural engineering, ocean engineering, and seismic engineering [26–29].

As a concrete form of PIDL paradigm, by embedding physical equations into traditional LSTM as regularization terms, the PI-LSTM model can be effectively applied to the predictions of complex dynamic systems [30]. Liu et al. [31] applied the PI-LSTM model to response modeling of the SDOF system and six-story building. Shi et al. [32] used PI-LSTM to model degradation trends of lithium-ion batteries and predict their remaining useful life, taking into account battery health and operating conditions. The fusion of data and physics effectively enhances the interpretability of the PI-LSTM model while reducing its reliance on labeled data [33]. In addition, PI-LSTM model also has unique advantages in dealing with inverse problems. It has great potential in the problems of parameter inversion and function inversion.

In this paper, a PI-LSTM model was constructed to address the forward and inverse problems of the frame structure equipped with the base isolation-fluid inerter system (FS-BIFI), and the damping-related parameters β_1, β_2 and a stiffness-related parameter μ of the fluid inerter are unknown. The structure and main contents of this paper are as follows: In Section 2, the fundamental structure and principle of the PI-LSTM model were provided. In Section 3, the reliability of the PI-LSTM model was validated by using a numerical case study of a single-story FS-BIFI. In Section 4, the PI-LSTM model was applied to a three-story FS-BIFI, achieving response prediction and parameters estimation. Finally, the primary conclusions of this paper were presented in Section 5.

2. PI-LSTM model for the FS-BIFI

Recurrent neural network (RNN) is a type of neural network utilized for processing sequential data. Among these, LSTM is a specific type of RNN designed primarily to address the vanishing and exploding gradient problems encountered during the training of long sequences. By embedding the equations of motion into a standard LSTM model, the PI-LSTM model is established for response prediction and parameters estimation of a complex structure.

Table 1
The training algorithm of the PI-LSTM model.

The training algorithm
Input: $\boldsymbol{I} = [\ddot{a}_g, \boldsymbol{u}]$
Initalize: $\boldsymbol{w}$, $\boldsymbol{b}$, λ
for $i = 1$ **to** *iterations* **do**
$\tilde{\boldsymbol{u}} = \textbf{PI\_LSTM}(\ddot{a}_g)$
$\text{Loss} = \text{Loss}_{\text{phy}} + \text{Loss}_{\text{data}}$
$(\boldsymbol{w}, \boldsymbol{b}, \boldsymbol{\lambda})^* = \arg\min_{(\boldsymbol{w},\boldsymbol{b},\boldsymbol{\lambda})}(\text{Loss})$
end
Save: $(\boldsymbol{w}, \boldsymbol{b}, \boldsymbol{\lambda})^*$
Output: $\tilde{\boldsymbol{u}}$

For a complex structural vibration problem, the physical equations can be represented as:

$$\begin{cases} N(f;\lambda) = 0 \\ BC(f;\lambda) = 0 \\ IC(f;\lambda) = 0 \end{cases} \tag{1}$$

Here, $f(x, \lambda)$ represents the implicit solution of the equations (structural response), and $x = (x_1, x_2, \ldots, x_n)$ is the input excitation. $N(\cdot;\lambda)$ is a nonlinear operator dependent on λ, while $BC(\cdot;\lambda)$ and $IC(\cdot;\lambda)$ denote the boundary and initial conditions, respectively.

The PI-LSTM model for the response prediction and parameters estimation for the aforementioned complex structural system depicted in Fig. 1. The PI-LSTM model mainly comprises two major components: a standard LSTM model and physical regularization terms. The LSTM model, serving as continuously differentiable approximation functions, are employed to establish the mapping relationship between input and output variables. The physical regularization term is utilized to analyze whether the input and output of the LSTM model adhere to the equations of motion. The automatic differentiation (AD) algorithm is used to compute the residuals of the equations of motion. The loss function of PI-LSTM model is composed of residuals from both data and physical equations, as depicted in Eq. (2). If there are unknown parameters λ in the equations, they are used as the parameters to be trained in the neural network. *TensorFlow-Adam Optimizer* [34] is employed to achieve

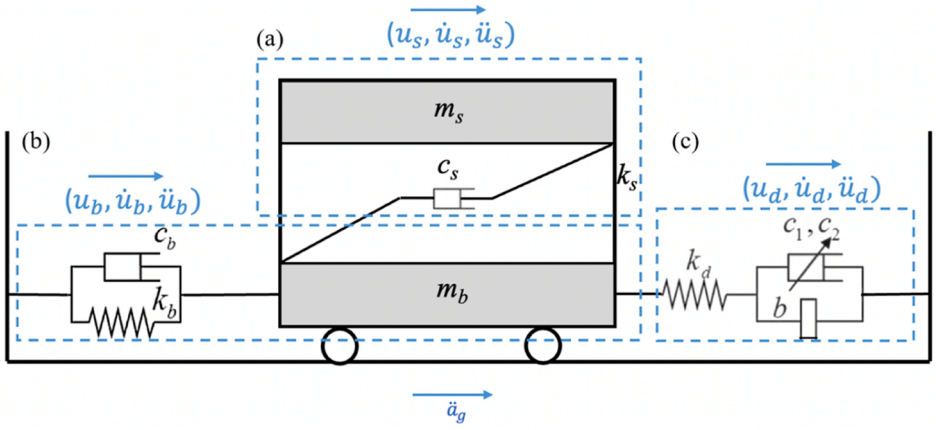

Fig. 2. The single-story FS-BIFI. (a) The superstructure; (b) The isolation layer; (c) The fluid inerter.

automatic gradient descent during the training process of PI-LSTM model. It rapidly updates the weight matrix (w), bias coefficients (b), and unknown parameters λ until minimizing the loss function. The training algorithm of the PI-LSTM model is shown in Table 1.

$$\begin{aligned} L_{total} &= L_{data} + L_{phy} \\ &= \|\widetilde{f} - f\| + \|N(\widetilde{f}, \lambda)\| + \|BC(\widetilde{f}, \lambda)\| + \|IC(\widetilde{f}, \lambda)\| \end{aligned} \tag{2}$$

Here, $\widetilde{f}$ represents the output of the LSTM model, while L_{data} and L_{phy} denote the residuals originating from the label data and the physical equations, respectively.

3. Model validation based on numerical case

To validate the effectiveness of the established PI-LSTM model, this section conducts response prediction and parameters estimation for a single-story FS-BIFI.

3.1. The model of a single-story FS-BIFI

As shown in Fig. 2, the base isolation-fluid inerter hybrid control structural system consists of three components: superstructure (see Fig. 2(a), subscript s), isolation layer (see Fig. 2(b), subscript b) and fluid inerter (see Fig. 2(c), subscript d). Wherein, the mechanical model of the fluid inerter can be simplified as depicted in Fig. 2(c), and its equation of motion can be represented as:

$$b\ddot{u} + c_1\dot{u}^2 + c_2\dot{u}^{1.75} + k_d u = 0 \tag{3}$$

Here, u is the displacement, b represents the inertance, c_1 and c_2 are nonlinear damping coefficients, and k_d is the equivalent bulk modulus, and can be obtained as following:

$$\begin{cases} b = \dfrac{\rho l A_1^2}{A_2} \\ k_d = \dfrac{1}{\dfrac{1}{K_{\text{liquid}}} + \dfrac{1}{100}\dfrac{1}{K_{\text{air}}}} \left(\dfrac{1}{L/2 - x} + \dfrac{1}{L/2 + x}\right) A_1 \\ c_1 = 0.0160 \dfrac{\rho l}{R^{0.5}} \dfrac{A_1^3}{A_2^{2.25}} \\ c_2 = 0.1376 \nu^{0.25} \rho^{0.75} l \dfrac{A_1^{2.75}}{A_2^{2.375}} \end{cases} \tag{4}$$

Where, A_1 is the working area of the cylinder, A_2 is the working area of the helical tube, l is the total length of the helical tube, R is the rotation radius of helical tube, L is the effective length of cylinder, ν and ρ are the viscosity coefficient and density of liquid, K_{liquid} and K_{air} are the bulk modulus of liquid and air.

Table 2
The relevant parameters of the structural model.

Physical variables	Value
m_s (10^3 kg)	3300
k_s (MN/m)	521.192
ξ	0.05
m_b (10^3 kg)	613
k_b (MN/m)	17.142
c_b (10^6 N•s/m)	1.63

Table 3
The relevant parameters of the fluid inerter.

Physical variables	Value
L (m)	1.0
l (m)	28.7
R (m)	0.618
A_1 (m^2)	0.718
A_2 (m^2)	0.005
ρ (kg/m^3)	1000
ν (cm^2/s)	0.001

For the single-story FS-BIFI, its normalized equations of motion can be expressed as:

$$\begin{aligned} &\ddot{u}_s + \alpha_1(\dot{u}_s - \dot{u}_b) + \alpha_2(u_s - u_b) + \ddot{a}_g = 0 \\ &\ddot{u}_b + \alpha_3\dot{u}_b + \alpha_4 u_b - \left[\alpha_5(\dot{u}_s - \dot{u}_b) + \alpha_6(u_s - u_b)\right] - \alpha_7(u_d - u_b) + \ddot{a}_g = 0 \\ &\ddot{u}_d + \beta_1|\dot{u}_d|^2\text{sgn}(\dot{u}_d) + \beta_2|\dot{u}_d|^{1.75}\text{sgn}(\dot{u}_d) + \mu\left(u_d - u_b\right) = 0 \end{aligned} \tag{5}$$

Where, $[\alpha_1, \alpha_2] = m_s^{-1}[c_s, k_s]$, $[\alpha_3, \alpha_4, \alpha_5, \alpha_6, \alpha_7] = m_b^{-1}[c_b, k_b, c_s, k_s, k_d]$, $[\beta_1, \beta_2, \mu] = b^{-1}[c_1, c_2, k_d]$. m, u, c, and k are the mass, displacement, damping and stiffness respectively, ξ is the damping ratio of the structure, and subscripts s, b and d are superstructure, isolation layer and fluid inerter respectively. The relevant parameters of the structural model and the fluid inerter adopted in this section are shown in Tables 2 and 3.

To generate labeled data for training PI-LSTM model, it is necessary to compute the structural response under various seismic excitations, simulating sparse data collected by sensors in real engineering scenarios. The *Newmark-β* method is employed to solve the structural response, and $\beta = 0.5$, $\gamma = 1/6$, the time step is 0.02 s. For further details, please refer to [35].

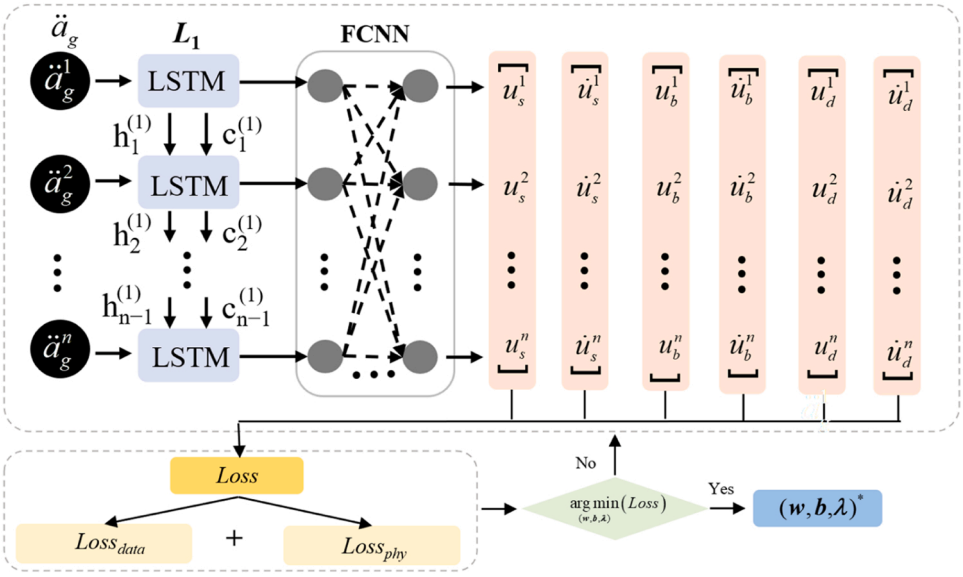

Fig. 3. The PI-LSTM model for analyzing the single-story FS-BIFI.

Table 4
The hyperparameters of the PI-LSTM model.

Hyper parameter	Value	Hyper parameter	Value
LSTM layers	1	Gradient threshold	1
Number of hidden nodes	{50,100,200}	Learning rate	0.01
FCNN layers	2	Optimizer	Adam
Neurons in FCNN layers	100	β_1	0.9
Batch size	{1,2,4,8,16,48}	β_2	0.999
Forgetting rate	0.06	ε	1.00E-7

Table 5
Configuration of platform for model training.

Configuration	Performance indicators
System	Windows 10 64-bit
CPU	Intel® Core™ i7-10875 H 2.35 GHz
GPU	NVIDIA GeForce RTX 2060 Max-Q 6 GB
RAM	64 G
Python	3.8.5
Tensorflow	1.6.0

3.2. PI-LSTM model construction and training

3.2.1. Model construction

Constructing a PI-LSTM model for response prediction and parameters estimation of the single-story FS-BIFI (as shown in Fig. 3). The calculation of the physical loss function requires displacement, velocity and acceleration responses (see Eq. (5)). In order to reduce the data burden, take any two indicators of displacement, velocity and acceleration, and use *Newmark-β* to get another indicator. In this case, the input of the LSTM model is the seismic acceleration $\ddot{a}_g = [\ddot{a}_g^1, \ddot{a}_g^2, \ldots, \ddot{a}_g^n]$, and its output is the structural displacement and velocity response $[u_s, \dot{u}_s, u_b, \dot{u}_b, u_d, \dot{u}_d]$ and the unknown parameters $\lambda = [\beta_1, \beta_2, \mu]$ of the fluid inerter. To ensure training convergence, the PI-LSTM model is composed of a single LSTM layer followed by 2 fully connected layers. The number of hidden nodes and the batch size are set as variable hyperparameters. The loss function consists of both physical residual and data residual, calculated using L2 regularization, as depicted in Eqs. (6) and (7). The learning rate is set to 0.01, the forget rate is set to 0.06, the gradient threshold is set to 1, and iterations is set to 500, as shown in Table 4.

$$L_{data} = \sum_i^N \left(\left\| \tilde{u}_s^i - u_s^i \right\| + \left\| \tilde{u}_b^i - u_b^i \right\| + \left\| \tilde{u}_d^i - u_d^i \right\| + \left\| \tilde{\dot{u}}_s^i - \dot{u}_s^i \right\| + \left\| \tilde{\dot{u}}_b^i - \dot{u}_b^i \right\| + \left\| \tilde{\dot{u}}_d^i - \dot{u}_d^i \right\| \right) \tag{6}$$

$$L_{phy} = \sum_i^N \left(\begin{array}{l} \left\| \frac{d\tilde{\dot{u}}_s^i}{dt} + \alpha_1 \left(\tilde{\dot{u}}_s^i - \tilde{\dot{u}}_b^i \right) + \alpha_2 \left(\tilde{u}_s^i - \tilde{u}_b^i \right) + \tilde{\ddot{a}}_g^i \right\| \\ + \left\| \frac{d\tilde{\dot{u}}_b^i}{dt} + \alpha_3 \tilde{\dot{u}}_b^i + \alpha_4 \tilde{u}_b^i - \left[\alpha_5 \left(\tilde{\dot{u}}_s^i - \tilde{\dot{u}}_b^i \right) + \alpha_6 \left(\tilde{u}_s^i - \tilde{u}_b^i \right) \right] - \alpha_7 \left(\tilde{u}_d^i - \tilde{u}_b^i \right) + \tilde{\ddot{a}}_g^i \right\| \\ + \left\| \frac{d\tilde{\dot{u}}_d^i}{dt} + \beta_1 \left| \tilde{\dot{u}}_d^i \right|^2 \mathrm{sgn}\left(\tilde{\dot{u}}_d^i \right) + \beta_2 \left| \tilde{\dot{u}}_d^i \right|^{1.75} \mathrm{sgn}\left(\tilde{\dot{u}}_d^i \right) + \mu \left(\tilde{\dot{u}}_d^i - \tilde{\dot{u}}_b^i \right) \right\| \\ + \left\| \frac{d\tilde{u}_s^i}{dt} - \tilde{\dot{u}}_s^i \right\| + \left\| \frac{d\tilde{u}_b^i}{dt} - \tilde{\dot{u}}_b^i \right\| + \left\| \frac{d\tilde{u}_d^i}{dt} - \tilde{\dot{u}}_d^i \right\| \end{array} \right) \tag{7}$$

Where the superscript (~) denotes the model's output, $\frac{d\tilde{\dot{u}}_s^i}{dt}$, $\frac{d\tilde{\dot{u}}_b^i}{dt}$, $\frac{d\tilde{\dot{u}}_d^i}{dt}$, $\frac{d\tilde{u}_s^i}{dt}$, $\frac{d\tilde{u}_b^i}{dt}$, $\frac{d\tilde{u}_d^i}{dt}$ are obtained through the *Newmark-β* method.

3.2.2. Model training

The seismic accelerations (60 original seismic accelerations + 582 seismic accelerations from incremental dynamic analysis) and

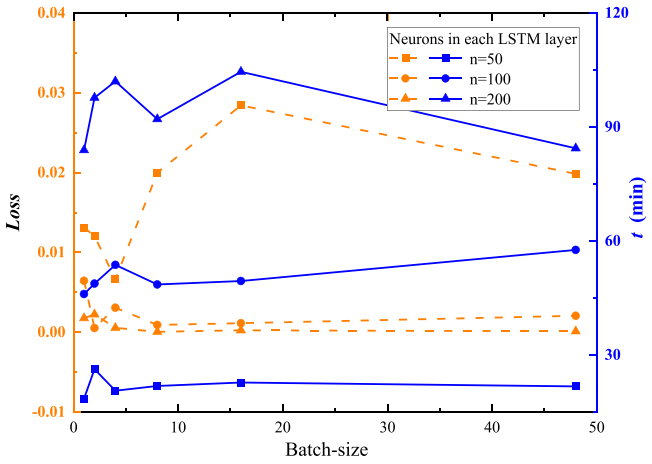

Fig. 4. The loss function and training time of the model with different parameters.

corresponding structural response from were selected in Ref. [35] as data sets. Based on the time series *k*-means algorithm (TSkmeans), the original seismic accelerations and incremental seismic accelerations are divided into three clusters, respectively. 80% of the three clusters of original seismic accelerations-structural response are randomly selected as the training set, a total of 48 groups of seismic accelerations-structural response. The rest of the data serves as the test set. The server platform and environment configuration used for all model training in this paper are shown in Table 5.

Fig. 4 demonstrates the effects of different training batch sizes and various numbers of hidden layer nodes on both the loss function and training time. As can be seen from Fig. 4, the number of hidden nodes and batch size have a great impact on the time and accuracy of model training. To balance computational efficiency and accuracy, this study employed a parameter configuration of $n = 100$ and a batch size of 2 to train the PI-LSTM model. The training iteration process of the model is shown in Fig. 5. It can be observed that at the conclusion of iterations, the data residual L_{data} and the physical residual L_{phy} are recorded as 1.01E-4 and 4.23E-4, respectively, which are within the same order of magnitude. This indicates that the PI-LSTM model is subject to a mutual constraint imposed by both physical equations and label data.

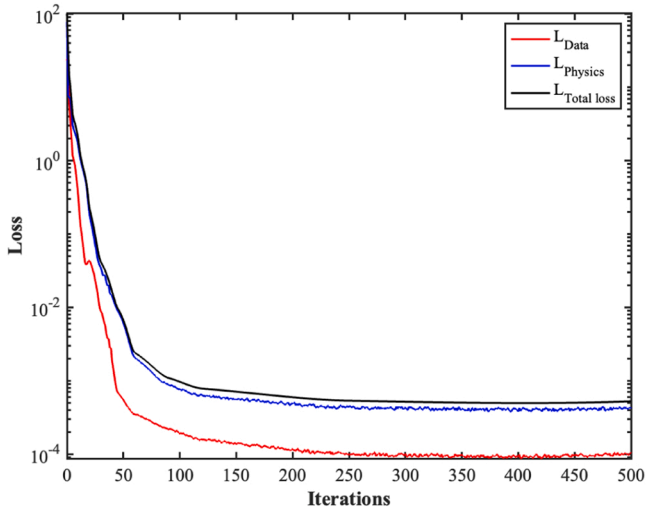

Fig. 5. The training iteration process of the PI-LSTM model.

3.3. Response prediction and parameters estimation

3.3.1. Response prediction

The probability density function (PDF) P_i is used to analyze the error of prediction results of three clusters test sets. The P_i is calculated as follows:

$$P_i = PDF\left\{\frac{(y_i - \widehat{y}_i)}{\max|(y_1, y_2, \ldots, y_n)|}\right\} \tag{8}$$

Where $\widehat{y}_i$ and y_i represent the predicted and numerical values, respectively. The weighted mean absolute percentage error (WMAPE) E_{WMAPE} and peak percentage error (PPE) E_{PEAK} are selected as evaluation indexes. The calculation formula is as follows:

$$E_{WMAPE} = \frac{1}{m \times n}\sum_{j=1}^{m}\sum_{i=1}^{n}\frac{|y_i - \widehat{y}_i|}{\max|(y_1, y_2, \ldots, y_n)|} \times 100\% \tag{9}$$

$$E_{PEAK} = \left|\frac{y_{peak} - \widehat{y}_{peak}}{y_{peak}}\right| \times 100\% \tag{10}$$

Where y_{peak} is the numerical peak value of the time history response, $\widehat{y}_{peak}$ is the predicted peak value of the time history response.

Fig. 6 shows the error distribution of prediction results by the PI-LSTM model. Table 6 shows the error values for displacement and velocity. As shown in Fig. 6(a), the errors of predicted result by using a test dataset comprising three clusters of seismic acceleration records, are mainly distributed within the range of ± 10%. It's evident that the PI-LSTM exhibits reliable feature learning abilities across diverse clusters of seismic motions, with confidence values of 96.58%, 95.74%, and 98.64%. Compared with data-driven LSTM model (90.2%, 86.7%, and 95.8% [35]), PI-LSTM model has improved the prediction accuracy of structural response under various clusters seismic excitation. u_d, $\dot{u}_d$, u_b, $\dot{u}_b$, u_s, $\dot{u}_s$ have confidence values within a range of ± 10% prediction error, which are 97.03%, 96.27%, 99.78%, 98.18%, 96.09%, and 99.55%, respectively (see Fig. 6(b)). Overall, the PI-LSTM model exhibits high predictive accuracy, with maximum WMAPE and PPE values of 5.101% and 5.245%, respectively (see Table 6).

Fig. 7 presents the predicted displacement and velocity time-history response of the superstructure, isolation layer and fluid inerter under the effect of a single seismic acceleration. The predicted responses for the superstructure, isolation layer and fluid inerter closely match the numerical results. This indicates that the PI-LSTM model exhibits outstanding accuracy in predicting vibration response of the single-story FS-BIFI, matching well with numerical results in both overall trends and local features. The PI-LSTM model can accurately capture the relationship between non-stationary segments of seismic excitations and the response characteristics of the single-story FS-BIFI.

3.3.2. Parameters estimation

During the completion of the aforementioned PI-LSTM model training process, the unknown parameters within the equations were concurrently estimated. Fig. 8 illustrates the trends of damping-related parameters β_1, β_2, and stiffness-related parameter μ during the training of the PI-LSTM model. It can be observed that the three curves show an initial increase followed by a decrease trend during the model training, eventually stabilizing at specific values. Ultimately, the estimated unknown parameter values are $\beta_1 = 11.343$, $\beta_2 = 5.154$ and $\mu = 10.021$. Based on the design parameters in Table 3, the actual damping-related parameters can be computed as $\beta_1 = 10.991$, $\beta_2 = 4.950$, and the stiffness-related parameter as $\mu = 9.706$. The relative errors are 3.202%, 4.121%, and 3.245%, respectively.

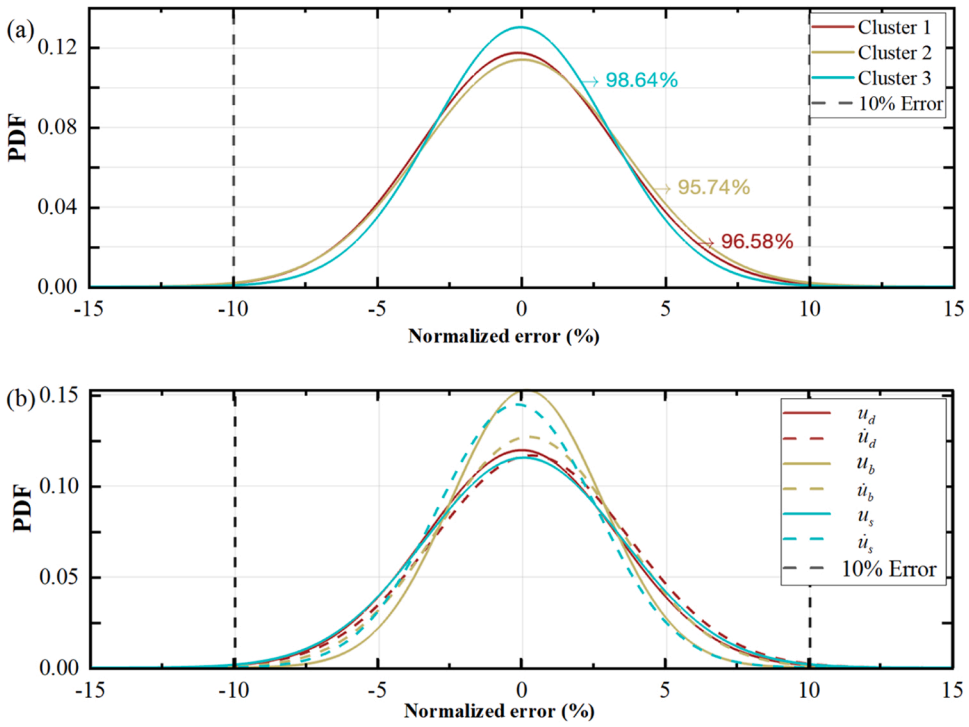

Fig. 6. The error distribution of prediction results by PI-LSTM mode. (a) Diverse clusters of seismic accelerations; (b) Diverse response metrics.

4. PI-LSTM for a frame structure model

4.1. Shaking table experiment of a three-story FS-BIFI

The superstructure is a three-story frame structure, and the column feet and frame joints are connected with angle steel or angle beam to ensure rigid connection. The rigid plates with a thickness of 20 mm are employed in each layer to ensure the superstructure exhibits significant lateral displacement and substantial out-of-plane stiffness. The dimensions of the floor slab are 1040 mm × 1040 mm × 20 mm, with a layer height of 950 mm, resulting in a total height of 2850 mm, as depicted in Fig. 9(a). Between the superstructure and the shaking table, a hybrid control system combining fluid inerter and anti-toppling rolling isolation is implemented, as depicted in Fig. 9(b). The data sampling frequency is 1000 Hz. The acquired data includes the shaking table displacement u_0, the absolute acceleration $\ddot{u}_{b\_abs}$ and the absolute displacement u_{b_abs} of the isolation layer, the absolute acceleration $\ddot{u}_{sj\_abs}$ and the absolute displacement u_{sj_abs} of each layer of the superstructure ($i = 1, 2, 3$), the output force of the fluid inerter, and the pressure of the helical tube. The relative acceleration and the relative displacement of the isolation layer can be obtained as $\ddot{u}_b = \ddot{u}_{b\_abs} - \ddot{a}_g$ and $u_b = u_{b\_abs} - u_0$. The relative acceleration and the relative displacement of the superstructure are $\ddot{u}_{sj} = \ddot{u}_{sj\_abs} - \ddot{a}_g$ and $u_{sj} = u_{sj\_abs} - u_0$.The fluid inerter is consolidated on the side of the supporting site of the isolation layer. The relative acceleration and the relative displacement of the fluid inerter are $\ddot{u}_d = \ddot{u}_b$ and $u_d = u_b$.

Based on the principle of mechanical equilibrium, the equations of motion for the three-layered framework structure with the isolation layer and the fluid inerter under the seismic excitation can be formulated as follows:

$$\begin{aligned}
&m_{s1}\ddot{u}_{s1} + c_{s1}\left(\dot{u}_{s1} - \dot{u}_{s2}\right) + k_{s1}\left(u_{s1} - u_{s2}\right) = -m_{s1}\ddot{a}_g \\
&m_{s2}\ddot{u}_{s2} + c_{s2}\left(\dot{u}_{s2} - \dot{u}_{s3}\right) + k_{s2}\left(u_{s2} - u_{s3}\right) - c_{s1}\left(\dot{u}_{s1} - \dot{u}_{s2}\right) - k_{s1}\left(u_{s1} - u_{s2}\right) = -m_{s2}\ddot{a}_g \\
&m_{s3}\ddot{u}_{s3} + c_{s3}\left(\dot{u}_{s3} - \dot{u}_b\right) + k_{s3}\left(u_{s3} - u_b\right) - c_{s2}\left(\dot{u}_{s2} - \dot{u}_{s3}\right) - k_{s2}\left(u_{s2} - u_{s3}\right) = -m_{s3}\ddot{a}_g \\
&m_b\ddot{u}_b + k_b u_b + F_s + F_b - \left[c_{s3}\left(\dot{u}_{s3} - \dot{u}_b\right) + k_{s3}\left(u_{s3} - u_b\right)\right] - k_d\left(u_d - u_b\right) = -m_b\ddot{a}_g \\
&b\ddot{u}_d + c_1|\dot{u}_d|^2 sgn(\dot{u}_d) + c_2|\dot{u}_d|^{1.75} sgn(\dot{u}_d) + k_d\left(u_d - u_b\right) = 0
\end{aligned} \tag{11}$$

Where the subscripts $s1$, $s2$, and $s3$ represent the top, second, and bottom layers of the framework structure. F_s and F_b denote the frictional damping of the rolling isolation and the isolation damping due to interaction forces between components, respectively. By employing the statistical linearization method, the equivalent damping coefficient c_{eq} of the rolling isolation can be derived as $F_s + F_b = c_{eq}\dot{u}_b$. Therefore, the equations of motion can be rewritten in the following form:

$$\begin{aligned}
&\ddot{u}_{s1} + \alpha_1\left(\dot{u}_{s1} - \dot{u}_{s2}\right) + \alpha_2\left(u_{s1} - u_{s2}\right) = -\ddot{a}_g \\
&\ddot{u}_{s2} + \alpha_3\left(\dot{u}_{s2} - \dot{u}_{s3}\right) + \alpha_4\left(u_{s2} - u_{s3}\right) - \alpha_5\left(\dot{u}_{s1} - \dot{u}_{s2}\right) - \alpha_6\left(u_{s1} - u_{s2}\right) = -\ddot{a}_g \\
&\ddot{u}_{s3} + \alpha_7\left(\dot{u}_{s3} - \dot{u}_b\right) + \alpha_8\left(u_{s3} - u_b\right) - \alpha_9\left(\dot{u}_{s2} - \dot{u}_{s3}\right) - \alpha_{10}\left(u_{s2} - u_{s3}\right) = -\ddot{a}_g \\
&\ddot{u}_b + \alpha_{11}\dot{u}_b + \alpha_{12}u_b - \alpha_{13}\left(\dot{u}_{s3} - \dot{u}_b\right) - \alpha_{14}\left(u_{s3} - u_b\right) - \alpha_{15}\left(u_d - u_b\right) = -\ddot{a}_g \\
&\ddot{u}_d + \beta_1|\dot{u}_d|^2 sgn(\dot{u}_d) + \beta_2|\dot{u}_d|^{1.75} sgn(\dot{u}_d) + \mu\left(u_d - u_b\right) = 0
\end{aligned} \tag{12}$$

Among them, $\alpha = [\alpha_1, \alpha_2, \ldots, \alpha_{15}]$ represent the normalized damping-related parameters and stiffness-related parameters, which can be obtained by calculating the parameters in Table 7. The design parameters of the fluid inerter are shown in Table 8. The damping-related parameters β_1 and β_2, as well as the stiffness-related parameter μ, of the fluid inerter are unknown parameters to be estimated and outputted through the PI-LSTM model.

4.2. PI-LSTM model construction and training

Establishing a PI-LSTM model for predicting response and evaluating parameters of the frame structure model based on the framework out-

Table 6
The predicted error of the PI-LSTM model.

		u_d	$\dot{u}_d$	u_b	$\dot{u}_b$	u_s	$\dot{u}_s$
Cluster 1	E_{PEAK}/%	1.344	1.667	1.981	2.094	1.279	1.555
	E_{WMAPE}/%	2.727	1.818	2.242	1.287	1.967	1.800
Cluster 2	E_{PEAK}/%	1.565	2.378	2.094	2.899	2.543	1.822
	E_{WMAPE}/%	4.149	4.313	5.101	3.652	5.245	3.473
Cluster 3	E_{PEAK}/%	0.900	1.235	1.011	0.879	0.992	1.376
	E_{WMAPE}/%	1.464	0.746	0.999	1.756	2.461	1.131

lined in Fig. 1. Different from the model in Section 3.2.1, the input of the PI-LSTM model is seismic excitation $\ddot{a}_g = [\ddot{a}_g^1, \ddot{a}_g^2, \ldots, \ddot{a}_g^n]$ and the output is displacement and acceleration response $[u_{s1}, \ddot{u}_{s1}, u_{s2}, \ddot{u}_{s2}, u_{s3}, \ddot{u}_{s3}, u_b, \ddot{u}_b, u_d, \ddot{u}_d]$. Due to differences in the structural equations of motion and the types of collected data, the loss function of the model can be represented as:

$$L_{phy} = \sum_i^N \left(\begin{array}{c} \|\ddot{\widetilde{u}}_{s1} + \alpha_1\left(\frac{d\widetilde{u}_{s1}}{dt} - \frac{d\widetilde{u}_{s2}}{dt}\right) + \alpha_2\left(\widetilde{u}_{s1} - \widetilde{u}_{s2}\right) + \ddot{a}_g\| \\ +\|\ddot{\widetilde{u}}_{s2} + \alpha_3\left(\frac{d\widetilde{u}_{s2}}{dt} - \frac{d\widetilde{u}_{s3}}{dt}\right) + \alpha_4\left(\widetilde{u}_{s2} - \widetilde{u}_{s3}\right) - \alpha_5\left(\frac{d\widetilde{u}_{s1}}{dt} - \frac{d\widetilde{u}_{s2}}{dt}\right) - \alpha_6\left(\widetilde{u}_{s1} - \widetilde{u}_{s2}\right) + \ddot{a}_g\| \\ +\|\ddot{\widetilde{u}}_{s3} + \alpha_7\left(\frac{d\widetilde{u}_{s3}}{dt} - \frac{d\widetilde{u}_b}{dt}\right) + \alpha_8\left(\widetilde{u}_{s3} - \widetilde{u}_b\right) - \alpha_9\left(\frac{d\widetilde{u}_{s2}}{dt} - \frac{d\widetilde{u}_{s3}}{dt}\right) - \alpha_{10}\left(\widetilde{u}_{s2} - \widetilde{u}_{s3}\right) + \ddot{a}_g\| \\ +\|\ddot{\widetilde{u}}_b + \alpha_{11}\frac{d\widetilde{u}_b}{dt} + \alpha_{12}\widetilde{u}_b - \alpha_{13}\left(\frac{d\widetilde{u}_{s3}}{dt} - \frac{d\widetilde{u}_b}{dt}\right) - \alpha_{14}\left(\widetilde{u}_{s3} - \widetilde{u}_b\right) - \alpha_{15}\left(\widetilde{u}_d - \widetilde{u}_b\right) + \ddot{a}_g\| \\ +\|\ddot{\widetilde{u}}_d + \beta_1\left|\frac{d\widetilde{u}_d}{dt}\right|^2 \mathrm{sgn}\left(\frac{d\widetilde{u}_d}{dt}\right) + \beta_2\left|\frac{d\widetilde{u}_d}{dt}\right|^{1.75} \mathrm{sgn}\left(\frac{d\widetilde{u}_d}{dt}\right) + \mu\left(\widetilde{u}_d - \widetilde{u}_b\right)\| \\ + \sum_{j=1}^3 \|\frac{d^2\widetilde{u}_{sj}}{dt^2} - \ddot{\widetilde{u}}_{sj}^i\| + \|\frac{d^2\widetilde{u}_b}{dt^2} - \ddot{\widetilde{u}}_b^i\| + \|\frac{d^2\widetilde{u}_d}{dt^2} - \ddot{\widetilde{u}}_d^i\| \end{array} \right) \tag{13}$$

$$L_{data} = \sum_i^N \left(\sum_{j=1}^3 \left(\left\|\widetilde{u}_{sj}^i - u_{sj}^i\right\| + \left\|\ddot{\widetilde{u}}_{sj}^i - \ddot{u}_{sj}^i\right\| \right) + \|\widetilde{u}_b^i - u_b^i\| + \|\ddot{\widetilde{u}}_b^i - \ddot{u}_b^i\| \|\widetilde{u}_d^i - u_d^i\| + + \|\ddot{\widetilde{u}}_d^i - \ddot{u}_d^i\| \right) \tag{14}$$

Where , $\frac{d\widetilde{u}_d}{dt}$, $\frac{d^2\widetilde{u}_d}{dt^2}$, $\frac{d\widetilde{u}_b}{dt}$, $\frac{d^2\widetilde{u}_b}{dt^2}$ and $\frac{d\widetilde{u}_{sj}^i}{dt}$, $\frac{d^2\widetilde{u}_{sj}^i}{dt^2}$ (j = 1, 2, 3) are obtained through the *Newmark-β* method.

The training set and test set are 21 groups of seismic excitation-structural response, as shown in Table 9. The classification criteria for near-field and far-field seismic waves are based on a fault displacement of 20 km. The data sampling interval is 0.001 s, with a duration of 50 s

The computing platform and environment configuration are summarized in Table 5. The hyperparameters specific to the PI-LSTM model are presented in Table 4. The number of iterations is 500. The model training duration was 3h52m27s. The loss functions associated with the model training are illustrated in Fig. 10. L_{data} converges to 4.239E-4, L_{phy} ultimately converges to 4.537E-3, resulting in a total loss value of 4.961E-3.

4.3. Response prediction and parameters estimation

4.3.1. Response prediction

In order to evaluate the predictive accuracy of the PI-LSTM model, the results obtained from the *Newmark-β* method will be included for comparative analysis. The error distribution between the responses predicted by the PI-LSTM and *Newmark-β* methods and the actual experimental responses is shown in Fig. 11. Table 10 displays the WMAPE and PPE of predicted acceleration and displacement responses. Within the confidence interval [− 10%, 10%], the confidence values of the predicted error by the PI-LSTM model and *Newmark-β* method are 96.68% and 77.53%, respectively. The PPE in the prediction results by the PI-LSTM model is within 7%, demonstrating a high level of predictive accuracy, whereas the numerical simulation results exhibit PPE exceeding 50%. This result suggests that compared to *Newmark-β* method, PI-LSTM can more accurately capture the vibrational characteristics of the three-story FS-BIFI.

A subset of experimental results and corresponding predicted outcomes for the seismic excitation Loma Prieta-0.01 g are selected for comparative analysis, depicted in Fig. 12. It's observable that the PI-LSTM model exhibits a good fit to the experimental data, accurately predicting structural response waveform characteristics even during the non-stationary phases of vibration. However, when predicting displacement response, its accuracy is inferior to that of the acceleration response, resulting in an overall waveform shift. This is due to residual displacements in the structural model from prior experiments, which did not fully return to the ideal initial position before the current test.

Fig. 13 (a), (d) and (g) illustrate the acceleration responses of the top layer, isolation layer and fluid inerter under a single seismic excitation obtained from experimental testing, *Newmark-β* method, and the PI-LSTM model. Based on the experimental results, the relative errors of the results obtained by PI-LSTM model and *Newmark-β* method are calculated. The calculated relative error value is shown in Fig. 13 (b), (e) and (h). Additionally, for further illustration of the prediction results' effectiveness, detailed local plots are provided in Fig. 13 (c), (f) and (i). It can be observed that the structural response obtained using the *Newmark-β* method, while showing a similar overall trend to the experimental results, exhibits considerable errors and neglects certain local minor high-frequency vibration characteristics. However, the PI-LSTM model, integrating structural equations of motion and experimental data, captures the minor high-frequency characteristics of structural vibrations. Hence, the results from the PI-LSTM model exhibit a high level of consistency with the experimental results.

4.3.2. Parameters estimation

Based on the design parameters in Table 8, the theoretical damping-related parameters β_1 and β_2 of the fluid inerter are 35.310 and 25.303, and the theoretical stiffness-related parameter μ is 419.95. The estimation β_1, β_2 and μ of the fluid inerter are 39.81567, 27.54401, and 404.23368, with corresponding relative errors of 12.760%, 8.857%, and 3.750% respectively (as shown in Fig. 14). The error in the damping-related parameter β_1 is comparatively larger than that of the damping-related parameter β_2 and the stiffness-related parameter μ. The main reason lies in the theoretical modeling overlooking factors such as frictional damping between the piston rod and the cylinder wall, pressure drops at the inlet and outlet, as well as machining errors.

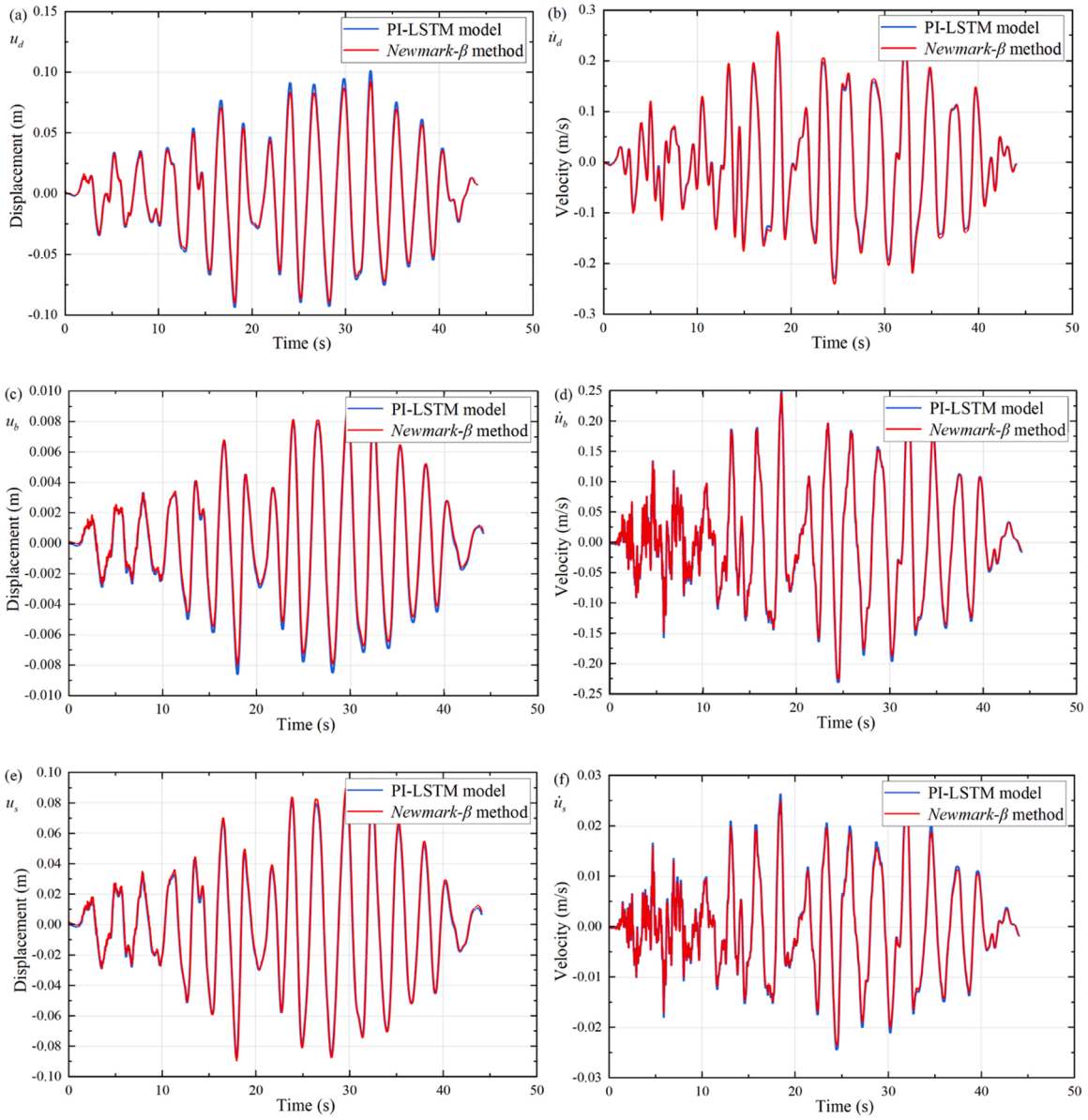

Fig. 7. The comparison between predicted and numerical results. (a) The displacement u_b; (b) The velocity $\dot{u}_b$; (c) The displacement u_d; (d) The velocity $\dot{u}_d$;(e) The displacement u_s; (f) The velocity $\dot{u}_s$.

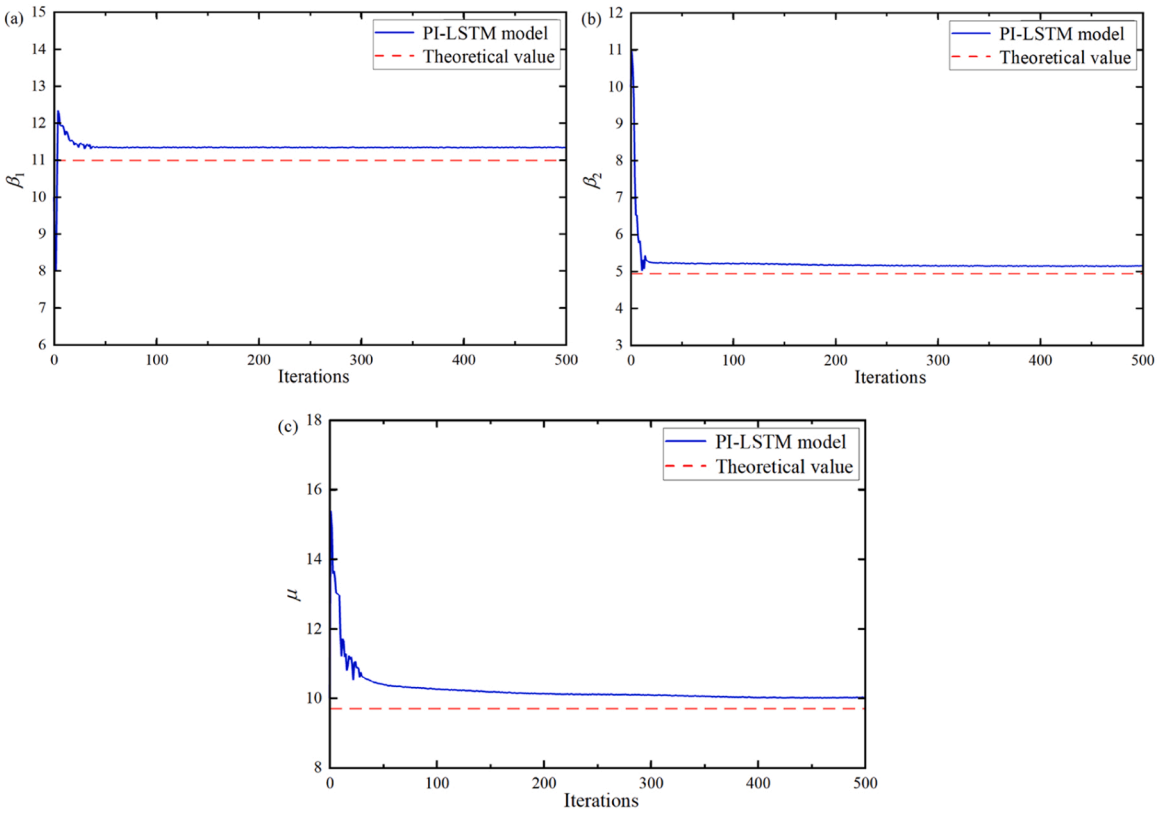

Fig. 8. The estimation results of unknown parameters of the fluid inerter. (a) The damping-related parameters β_1; (b) The damping-related parameters β_2; (c) The stiffness-related parameter μ.

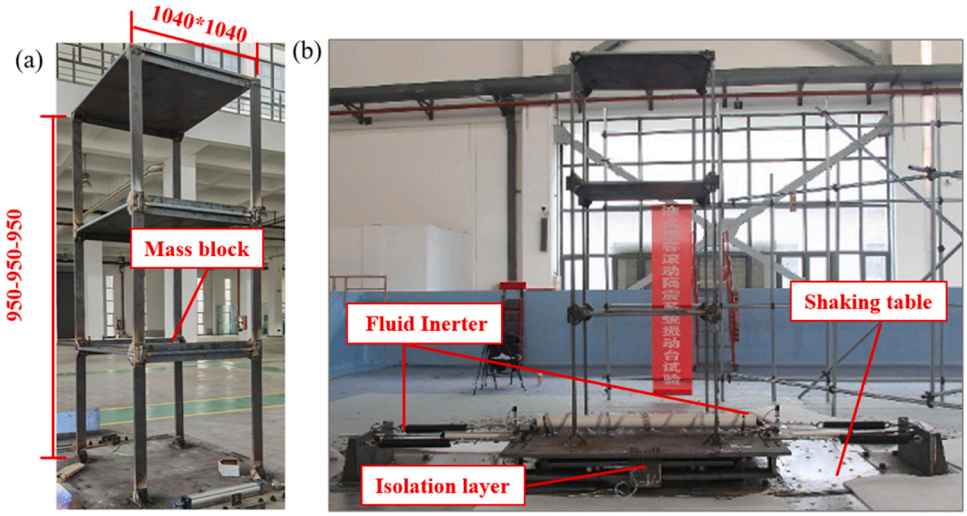

Fig. 9. The shaking table experiment of a three-story FS-BIFI. (a) The FS-BIFI; (b) The shaking table experiment.

Table 7
The parameters of the structural model.

Physical variables	Value	Physical variables	Value
m_{s1} (kg)	300	m_{s3} (kg)	300
k_{s1} (kN/m)	466.740	k_{s3} (kN/m)	466.740
c_{s1} (N·s/m)	2659	c_{s3} (N·s/m)	5318
m_{s2} (kg)	300	m_b (kg)	950
k_{s2} (kN/m)	466.740	k_b (kN/m)	476.900
c_{s2} (N·s/m)	2659	c_{eq} (kN/m)	1937

Table 8
The relevant parameters of the fluid inerter.

Physical variables	Value
L (m)	0.6
l (m)	4
R (m)	0.0365
A_1 (m^2)	3.117E-3
A_2 (m^2)	7.854E-5
ρ (kg/m^3)	1000
ν (cm^2/s)	0.001

Table 9
Training set and test set.

Data set	No.	Seismic excitation	Type	Amplitude (g)
Training set	1	EL-Centro	near-field	0.05
	2	Chi-Chi	near-field	0.05
	3	Loma Prieta	near-field	0.05
	4	San Fernando	far-field	0.05
	5	White Noise-01	white noise	0.05
	6	EL-Centro	near-field	0.10
	7	Livermore-01	far-field	0.10
	8	Tabas, Iran	far-field	0.10
	9	San Fernando	far-field	0.10
	10	White Noise-02	white noise	0.05
	11	Chi-Chi	near-field	0.20
	12	Loma Prieta	near-field	0.20
	13	Tabas, Iran	far-field	0.20
	14	Livermore-01	far-field	0.20
Test set	1	Livermore-01	far-field	0.05
	2	Tabas, Iran	far-field	0.05
	3	Chi-Chi	near-field	0.10
	4	Loma Prieta	near-field	0.10
	5	EL-Centro	near-field	0.20
	6	San Fernando	far-field	0.20
	7	White Noise-03	white noise	0.05

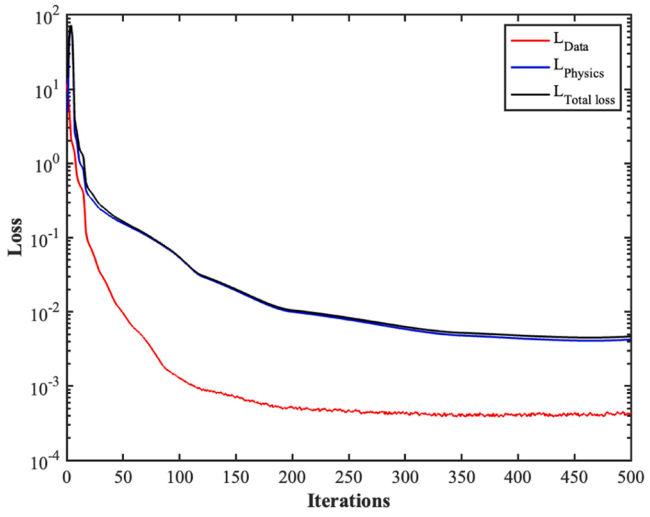

Fig. 10. The training iteration process of the PI-LSTM model.

In summary, as numerical methods solely address the structural equations of motion without considering influential factors like material properties and temperature existed in experiments, the computed results demonstrate substantial discrepancies from experimental results. Conversely, the PI-LSTM model, integrating structural equations of motion with experimental response data, exhibits a remarkably close alignment with experimental results in both overall trends and specific local details.

5. Conclusion

In this paper, the PI-LSTM model is used to predict response and estimate unknown parameters of the FS-BIFI. The applicability of PI-LSTM model to response prediction and parameters estimation is verified based on a numerical case study of a single-story FS-BIFI. Then, the response of a three-story FS-BIFI in the shaking table is predicted, and the unknown parameters of the fluid inerter are estimated. The main conclusions are obtained as follows:

(1) The PI-LSTM model, designed for the response prediction and parameters evaluation of the complex structure, is developed by embedding the structural equations of motion as a regularization term within the LSTM model. The applicability of the PI-LSTM model is validated based on a numerical case study of a single-story FS-BIFI. The predicted responses u_d, $\dot{u}_d$, u_b, $\dot{u}_b$, u_s, and $\dot{u}_s$ have confidence values within a range of $\pm$ 10% prediction error, which are 97.03%, 96.27%, 99.78%, 98.18%, 96.09%, and 99.55%, respectively. The evaluation unknown parameter values are $\beta_1 = 11.343$, $\beta_2 = 5.154$ and $\mu = 10.021$, and the corresponding relative errors are 3.202%, 4.121% and 3.245%, respectively.

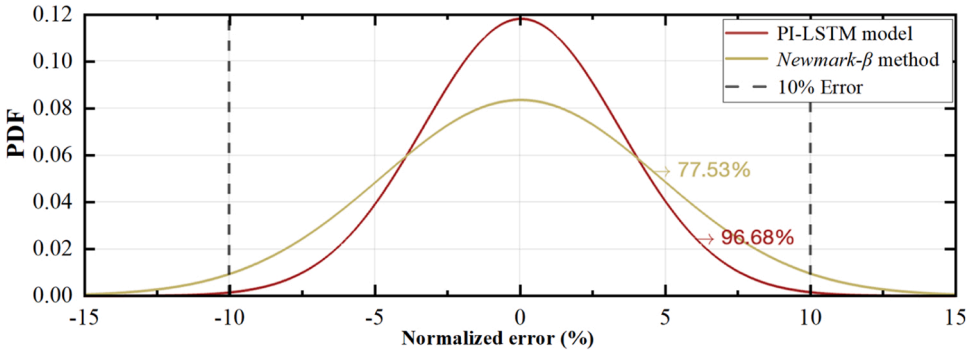

Fig. 11. The error distribution of prediction results by PI-LSTM model and *Newmark-β* method.

Table 10
The error of the PI-LSTM model and *Newmark-β* method.

		$\ddot{u}_b$	$\ddot{u}_d$	$\ddot{u}_{s1}$	u_b	u_d	u_{s1}
PI-LSTM	E_{PEAK}/%	2.722	3.094	6.368	4.113	2.498	8.544
	E_{WMAPE}/%	1.484	1.491	1.084	0.979	0.977	4.424
Newmark-β	E_{PEAK}/%	59.426	57.609	63.685	56.668	57.102	70.125
	E_{WMAPE}/%	6.029	7.523	14.360	4.925	4.899	23.701

(2) The PI-LSTM model is employed to predict the response of a three-story FS-BIFI situated on the shaking table. Within the confidence interval [− 10%, 10%], the confidence values of the predicted error by the PI-LSTM model and *Newmark-β* method are 96.68% and 77.53%, respectively. The PPE of the prediction results by the PI-LSTM model is within 7%, demonstrating a high level of predictive accuracy, whereas the numerical simulation results exhibit PPE exceeding 50%.

(3) The PI-LSTM model is employed to estimate unknown parameters of the fluid inerter mounted on the FS-BIFI. The evaluation damping-related parameters β_1 and β_2 of the fluid inerter are 39.81567 and 27.54401, and the evaluation stiffness-related parameter μ is 404.23368. The corresponding relative errors are 12.760%, 8.857%, and 3.750% respectively.

The current research employs a data- and physics-driven LSTM model to predict the nonlinear time history response of complex

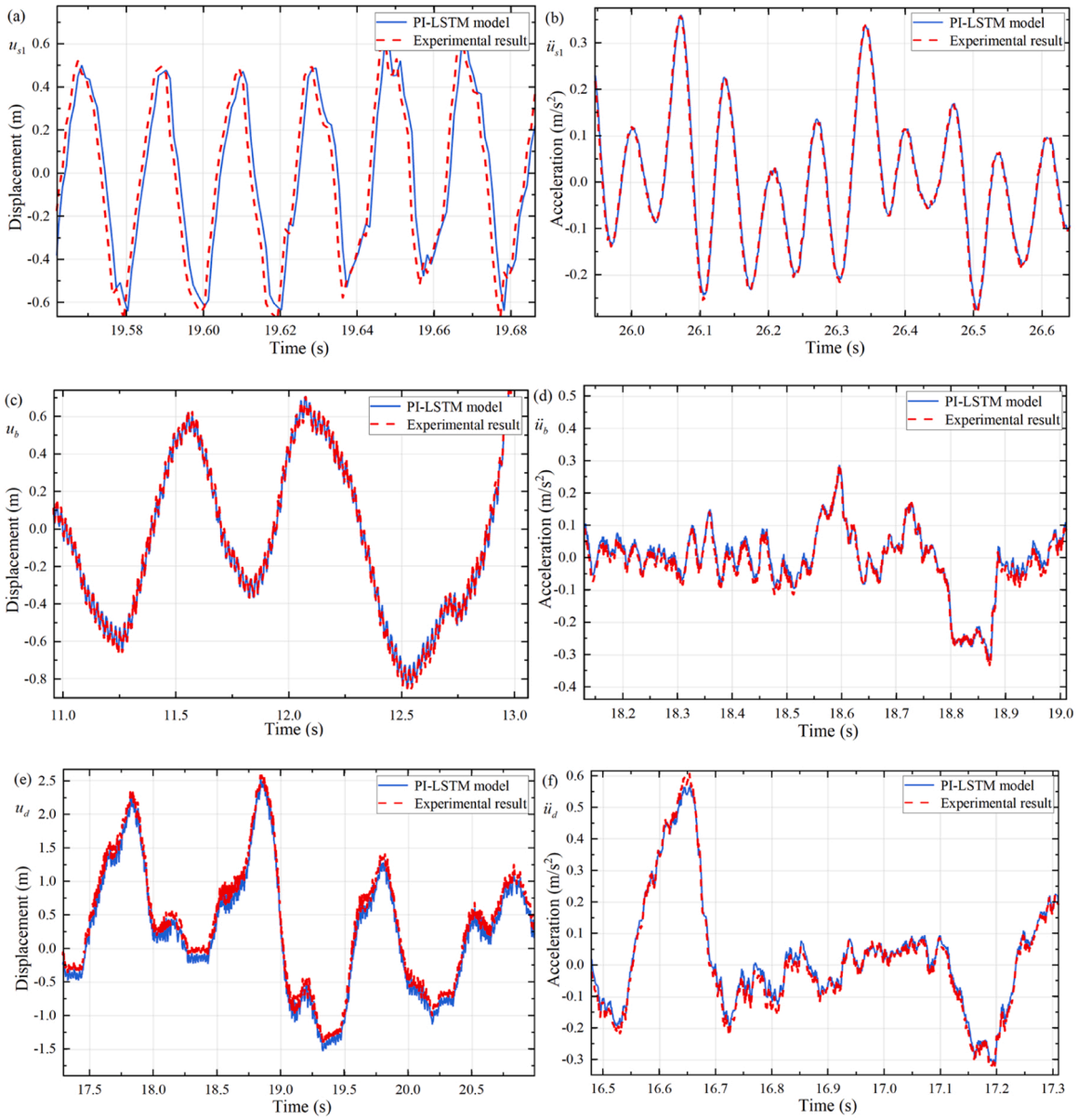

Fig. 12. The experimental results and corresponding predicted outcomes for the seismic excitation Loma Prieta-0.01 g. (a) The displacement u_{s3}; (b) The acceleration $\ddot{u}_{s3}$; (c) The displacement u_b; (d) The acceleration $\ddot{u}_b$; (e) The displacement u_d; (f) The acceleration $\ddot{u}_d$.

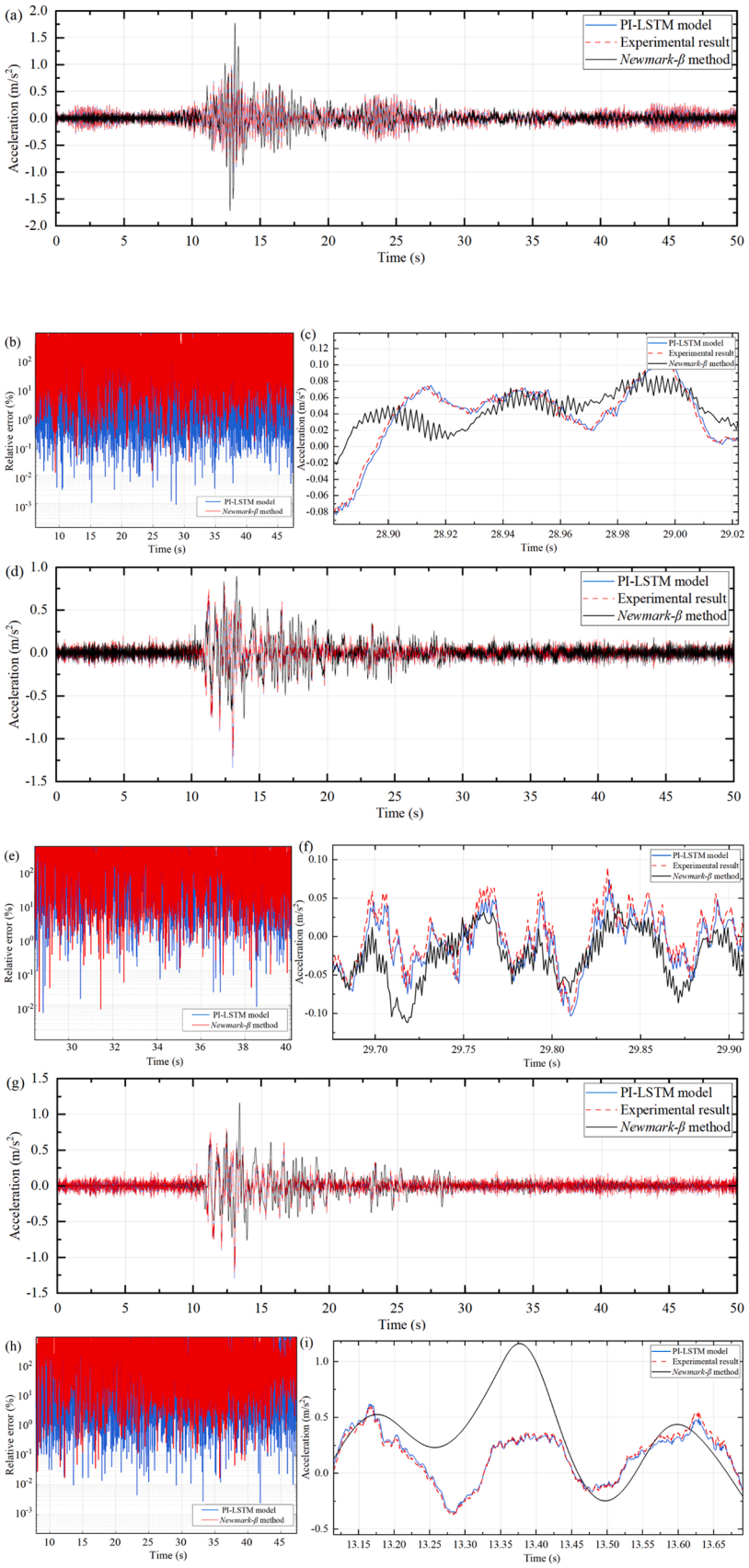

Fig. 13. The comparison of structural responses calculated by different methods. (a) The acceleration $\ddot{u}_{s3}$; (b) The relative error of $\ddot{u}_{s3}$; (c) The local detailed diagram of $\ddot{u}_{s3}$; (d) The acceleration $\ddot{u}_b$; (e) The relative error of $\ddot{u}_b$; (f) The local detailed diagram of $\ddot{u}_b$; (g) The acceleration $\ddot{u}_d$; (h) The relative error of $\ddot{u}_b$; (i) The local detailed diagram of $\ddot{u}_b$.

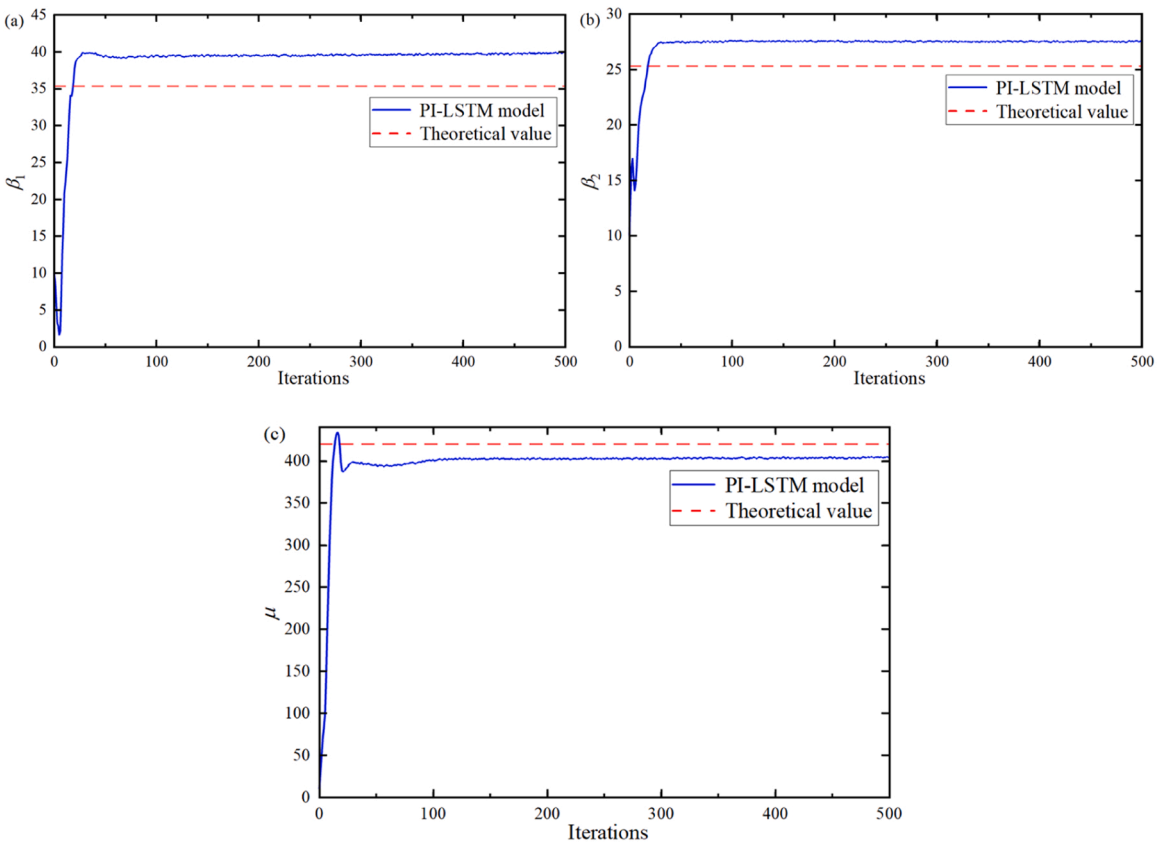

Fig. 14. The estimation results of unknown parameters for the experimental model. (a) The damping-related parameters β_1; (b) The damping-related parameters β_2; (c) The stiffness-related parameter μ.

structures with unknown parameters under seismic excitation. Simultaneously, it accurately achieved the evaluation of these unknown parameters. However, different structural models exhibit distinct temporal memory characteristics, corresponding to specific forms of equations-of-motion. This directly impacts the applicability of the PI-LSTM model. Therefore, in subsequent research, including the identification and prediction of other complex models, will be crucial. In addition, the weight ratio between the physical loss function and the data loss function of the PI-LSTM model is crucial. In order to further improve the generalization and stability of the model, the self-adaptive weight method should be adopted [25].

CRediT authorship contribution statement

Liyu Xie: Formal analysis, Writing – original draft. **Lingxiao Ran:** Formal analysis, Investigation, Writing – original draft. **Rongshuai Li:** Investigation, Supervision, Writing – review & editing. **Hesheng Tang:** Writing – original draft, Project administration, Methodology, Funding acquisition, Data curation, Conceptualization, Writing – review & editing. **Yangyang Liao:** Writing – review & editing, Writing – original draft, Supervision, Methodology, Investigation, Formal analysis, Conceptualization.

Declaration of Competing Interest

The authors declare that they have no known competing financial interests or personal relationships that could have appeared to influence the work reported in this paper.

Data Availability

Data will be made available on request.

Acknowledgments

This research was supported by National Natural Science Foundation of China (Grant No. 52378184), Shanghai Municipal Science and Technology Major Project (Grant No. 2021SHZDZX0100), National Key R&D Program of China (Grant No. 2021YFE0112200) and Ministry of Science and Technology of China (Grant No. SLDRCE19-B-02).

References

[1] Abbas M, Elbaz K, Shen SL, Chen J. Earthquake effects on civil engineering structures and perspective mitigation solutions: a review. Arab J Geosci 2021;14:1–17.
[2] Zhai C, Zhao Y, Wen W, Qin H, Xie L. A novel urban seismic resilience assessment method considering the weighting of post-earthquake loss and recovery time. Int J Disaster Risk Reduct 2023;84:103453.
[3] Swift SJ, Smith MC, Glover AR, Papageorgiou C, Gartner B, Houghton NE. Design and modelling of a fluid inerter. Int J Control 2013;86(11):2035–51.
[4] Liu C, Chen L, Lee HP, Yang Y, Zhang X. A review of the inerter and inerter-based vibration isolation: theory, devices, and applications. J Frankl Inst 2022;359(14):7677–707.
[5] Gürbüz M, Kocaman İ. Enhancing seismic resilience: a proposed reinforcement technique for historical minarets. Eng Fail Anal 2023:107832.
[6] Gönen S, Soyöz S. Seismic analysis of a masonry arch bridge using multiple methodologies. Eng Struct 2021;226:111354.
[7] Alam, Z., Sun, L., Zhang, C., & Samali, B. (2022, May). Influence of seismic orientation on the statistical distribution of nonlinear seismic response of the stiffness-eccentric structure. In Structures (Vol. 39, pp. 387–404). Elsevier.
[8] Wang, W., & Wang, X. (2023, August). Seismic behaviour of structures under long-duration ground motions: A review. In Structures (Vol. 54, pp. 1224–1236). Elsevier.
[9] Xu, F. , Bao, C. , Ma, X. , Zhang, Y. , Lim, K.S. , Zhang, Y. & et al. (2022, December). Shaking table test on seismic response of a planar irregular structure with differential settlements of foundation. In Structures (Vol. 46, pp. 988–999). Elsevier.
[10] Li Z, Huang G, Chen X, Zhou X. Seismic response and parametric analysis of inter-story isolated tall buildings based on enhanced simplified dynamic model. Int J Struct Stab Dyn 2022;22(03n04):2240008.

[11] Xiong M, Chen Z, Huang Y. Nonlinear stochastic seismic dynamic response analysis of submerged floating tunnel subjected to non-stationary ground motion. Int J Non-Linear Mech 2023;148:104270.
[12] Malik FN, Kolay C. Optimal parameters for tall buildings with a single viscously damped outrigger considering earthquake and wind loads. Struct Des Tall Spec Build 2023;32(7):e2003.
[13] Peng, H., Yan, J., Yu, Y., & Luo, Y. (2021, February). Time series estimation based on deep learning for structural dynamic nonlinear prediction. In Structures (Vol. 29, pp. 1016–1031). Elsevier.
[14] Wu RT, Jahanshahi MR. Deep convolutional neural network for structural dynamic response estimation and system identification. J Eng Mech 2019;145(1):04018125.
[15] Kundu A, Ghosh S, Chakraborty S. A long short-term memory based deep learning algorithm for seismic response uncertainty quantification. Probabilistic Eng Mech 2022;67:103189.
[16] Lake BM, Baroni M. Human-like systematic generalization through a meta-learning neural network. Nature 2023:1–7.
[17] Raissi M, Perdikaris P, Karniadakis GE. Machine learning of linear differential equations using Gaussian processes. J Comput Phys 2017;348:683–93.
[18] Raissi M, Karniadakis GE. Hidden physics models: Machine learning of nonlinear partial differential equations. J Comput Phys 2018;357:125–41.
[19] Raissi M, Perdikaris P, Karniadakis GE. Physics-informed neural networks: A deep learning framework for solving forward and inverse problems involving nonlinear partial differential equations. J Comput Phys 2019;378:686–707.
[20] Karniadakis GE, Kevrekidis IG, Lu L, Perdikaris P, Wang S, Yang L. Physics-informed machine learning. Nat Rev Phys 2021;3(6):422–40.
[21] Yang L, Meng X, Karniadakis GE. B-PINNs: Bayesian physics-informed neural networks for forward and inverse PDE problems with noisy data. J Comput Phys 2021;425:109913.
[22] Kharazmi E, Zhang Z, Karniadakis GE. hp-VPINNs: variational physics-informed neural networks with domain decomposition. Comput Methods Appl Mech Eng 2021;374:113547.
[23] Meng X, Li Z, Zhang D, Karniadakis GE. PPINN: parareal physics-informed neural network for time-dependent PDEs. Comput Methods Appl Mech Eng 2020;370:113250.
[24] Lu L, Meng X, Mao Z, Karniadakis GE. DeepXDE: a deep learning library for solving differential equations. SIAM Rev 2021;63(1):208–28.
[25] Ding Y, Chen S, Li X, Wang S, Luan S, Sun H. Self-adaptive physics-driven deep learning for seismic wave modeling in complex topography. Eng Appl Artif Intell 2023;123:106425.
[26] Raissi M, Wang Z, Triantafyllou MS, Karniadakis GE. Deep learning of vortex-induced vibrations. J Fluid Mech 2019;861:119–37.
[27] Tang H, Liao Y, Yang H, Xie L. A transfer learning-physics informed neural network (TL-PINN) for vortex-induced vibration. Ocean Eng 2022;266:113101.
[28] Hu Y, Tsang HH, Lam N, Lumantarna E. Physics-informed neural networks for enhancing structural seismic response prediction with pseudo-labelling. Arch Civ Mech Eng 2024;24(1):1–16.
[29] Haghighat E, Abouali S, Vaziri R. Constitutive model characterization and discovery using physics-informed deep learning. Eng Appl Artif Intell 2023;120:105828.
[30] Singh, S.K., Yang, R., Behjat, A., Rai, R., Chowdhury, S., & Matei, I. (2019, December). Pi-lstm: Physics-infused long short-term memory network. In 2019 18th IEEE International Conference On Machine Learning And Applications (ICMLA) (pp. 34–41). IEEE.
[31] Liu F, Li J, Wang L. PI-LSTM: Physics-informed long short-term memory network for structural response modeling. Eng Struct 2023;292:116500.
[32] Shi J, Rivera A, Wu D. Battery health management using physics-informed machine learning: online degradation modeling and remaining useful life prediction. Mech Syst Signal Process 2022;179:109347.
[33] Zhang, L. , Bellugi, D.G. , Li, S. , Kamat, A. , Kadi, J. , Moges, E. , & et al. (2022, December). A physics-informed machine learning model for streamflow prediction. In AGU Fall Meeting Abstracts (Vol. 2022, pp. H31E-01).
[34] Kingma, D.P., & Ba, J.L. Adam: a method for stochastic optimization. 3rd International Conference on Learning Representations, ICLR 2015-Conference Track Proceedings; 2015.
[35] Liao Y, Tang H, Li R, Ran L, Xie L. Response prediction for linear and nonlinear structures based on data-driven deep learning. Appl Sci 2023;13(10):5918.